

## N O T I C E

THIS DOCUMENT HAS BEEN REPRODUCED FROM  
MICROFICHE. ALTHOUGH IT IS RECOGNIZED THAT  
CERTAIN PORTIONS ARE ILLEGIBLE, IT IS BEING RELEASED  
IN THE INTEREST OF MAKING AVAILABLE AS MUCH  
INFORMATION AS POSSIBLE

# GRADUATE AERONAUTICAL LABORATORIES CALIFORNIA INSTITUTE OF TECHNOLOGY



(NASA-CR-176410) EFFECT OF STRESS  
CONCENTRATIONS IN COMPOSITE STRUCTURES  
Progress Report (California Inst. of Tech.)  
47 p HC A03/HF A01  
CSCL 11D

N86-15348

G3/24 Unclas  
04988

Firestone Flight Sciences Laboratory

Guggenheim Aeronautical Laboratory

Karman Laboratory of Fluid Mechanics and Jet Propulsion

Pasadena

SM REPORT 85-12

**EFFECT OF STRESS CONCENTRATIONS  
IN COMPOSITE STRUCTURES**

by

C.D Babcock\* and A.M. Waas\*\*

Graduate Aeronautical Laboratories  
California Institute of Technology  
Pasadena, CA 91125

Progress Report

NASA Grant: NSG 1483

November 1985

1. INTRODUCTION

Composite structures have found wide use in many engineering fields and a sound understanding of their response under load is important to their utilization. An experimental program is being carried out to gain a fundamental understanding of the failure mechanics of multilayered composite structures at GALCIT. As a part of this continuing study, we are interested in assessing the performance of laminated composite plates in the presence of a stress gradient and the failure of composite structures at points of thickness discontinuity. In particular we address the questions of initiation of failure and its subsequent growth to complete

---

\* Professor of Aeronautics and Applied Mechanics

\*\* Graduate Research Assistant

failure of the structure.

## 2. FAILURE INITIATION AND PROPAGATION IN THE PRESENCE OF A STRESS GRADIENT AND A FREE EDGE

For the experimental program studying the mechanisms of failure initiation and propagation it was desirable to know where the failure is most likely to initiate. For this reason a flat plate with a hole was chosen as a test structure. The hole is carefully cut in order to insure that excessive local damage does not occur during the machining process (Ref. 1). Compression loading is applied using a hydraulic jack.

The loading device and the optical components that are used in the experiments are mounted on a 5'x7' optical table with pneumatic vibration isolation. As reported earlier, Holographic Interferometry is used to capture the deformation occurring around the hole. One difficulty we encountered was the choice of a suitable recording medium for the interferograms. Real time studies were difficult due to the wet chemical processes involved in the developing of the photographic glass plates. Moreover, the time consumed between the exposures was excessive. We have successfully circumvented this difficulty by purchasing a newly developed thermoplastic instant recording device (manufactured by Honeywell Corp. with NRC as the marketing agent). A brief description of this follows.

### 2.1. The Instant Recording Device.

In the reconstruction process of a hologram the conventional silver halide photographic plates cause diffraction via an amplitude grating which is representative of the spatial distribution of the light (amplitude and phase) that is emitted from the diffusely reflective surface of the object. However, the same task could be accomplished with a phase-grating i.e., a surface contour variation which is representative of the reflected light off the object. This is the basic principle behind the

success of the thermoplastic recording device. The device has several stages of operation as shown in Fig.1. Steps a through d require less than 1 minute - a considerable saving of time. Furthermore, with real time Holographic Interferometry, a complete deformation history of the object up to failure can be recorded. This is important in the study of composites which exhibit several "stages" of failure. There are four basic steps in the creation of a hologram with this device.

Step 1.

A uniform charge is deposited on the plate as shown in Fig. 1a. A movable coronatron deposits this charge. A corresponding negative charge forms in the transparent electrical conductor which is connected to ground.

Step 2.

The plate is exposed. Charge passes through the photo conductor only in the illuminated areas (Fig. 1b).

Step 3.

Another charge is provided to the plate. Because the plate is now not exposed to the light the charge does not move across the photoconductor. Thus the areas of the thermoplastic that were illuminated experience a greater electric field; the charge density is greater in the illuminated areas.

Step 4

The development of the hologram is carried out by heating the thermoplastic plate. In areas where the electric field is greater, the heat softened thermoplastic becomes thinner (Fig. 1d). This creates the surface contour variation which causes the diffraction of light in the

reconstruction stage.

The coronatron is a device that consists of a wire anode running down the center of a slotted cylinder. The slot is oriented to face the thermoplastic plate. The slotted cylinder and the plate are grounded and the anode is raised to a potential of several kilovolts. The resulting electric fields ionize the surrounding air, producing electrons and positive ions. The electrons are collected on the wire which results in a positive charge on the slotted cylinder and the thermoplastic plate (Fig. 2).

The detailed structure of the thermoplastic plate is shown in Fig. 3. On a quartz substrate, an optically transparent electrode of indium-tin oxide is deposited on top of which a 1  $\mu\text{m}$  thick layer of trinitrofluorenone doped photoconductive organic polymer is placed and finally a 0.7  $\mu\text{m}$  thermoplastic layer is added. Metal electrodes are attached to each side of the transparent electrode which provides a ground plane for the coronatron. A current passed through the transparent electrode produces resistive heating sufficient to soften the thermoplastic.

The cycle of events explained above is sequenced by a control unit supplied with the recording device. Dry Nitrogen is used as the coolant for the thermoplastic plate in the erase process. This consists of reheating the thermoplastic to relieve it of the surface contour variation to produce a ripple-free surface. Upon cooling, the plate is ready to be used again in the formation of a hologram.

## 2.2. Specimens.

Test specimen are cut from the panels remaining from the impact delamination study. Diamond impregnated core drills and saws are used for cutting purposes. The geometry of the specimen is shown in Figure 4. The dimensions of the test specimens are chosen to induce failure due to the stress concentration effect prior to a global buckling failure of the plate. A number of specimen have been tested to failure. The complete

history of 2 of these has been recorded in the form of interferograms and will be discussed in detail. The plate fiber/matrix system is T300/5208 and are 48-ply with a stacking sequence  $(+ 45/90_2/+ 45/90_2/+ 45/90/0)_{2s}$  (angles are measured from the load axis). They are fabricated from uni-directional tape of Thornel 300 graphite fibers pre-impregnated with either matrix. The resin volume fraction and total laminate thickness are 28% and 6.1 mm for T300/5208 and 38% and 6.7 mm for T300/BP907 respectively.

Several of the T300/5208 specimens have been tested. Of the 2 specimens for which complete histories were recorded, one was tested with the stacking sequence given above. The other panel was cut with the load axis  $90^\circ$  to the indicated lay up.

### 2.3. Experimental Procedure.

A schematic of the holographic interferometer used in this study is shown in Figure 5. It is a standard off axis holographic system. Apart from a few double exposure holograms it is used for real time observations. Proper choice of reference to object beam intensity ratio is important for producing the best holograms. With the use of the instant recording device, the quality of the hologram is insensitive to the exposure time. In the real-time mode, the test specimen is illuminated in a state  $S_1$  (say) with coherent light transmitted from the laser via the object wave path (this consists of the beam splitter, a beam expander-spatial filter, collimating lens). A hologram is then recorded by exposing the thermoplastic plate positioned at the junction of the reflected light and reference beam. Upon completion of the 1st exposure the specimen is loaded and viewed through a camera attached to a VHS recording system. (a VCR and a monitor). The load is slowly increased, which, results in fringes which are dynamical in nature, since the load is continuously varying. These fringes, together with the load cell reading are recorded. The load cell reading is obtained by focussing the display of the voltmeter, exhibiting the load cell reading, at the position of the circular

hole in the plane of the test specimen. Thus a typical frame would look like that displayed in Figure 6. When the fringe density becomes high, the resolution of the interferogram becomes poorer. At this stage a new hologram of the test specimen is made and the above cycle of events is repeated. Thus, finally at the end of each experiment we obtain an interferometric recording of the complete load out-of-plane displacement history of the specimen.

Each of the holographic interference fringe field is related to the change in surface displacement of the specimen under load, by the vector expression

$$n\lambda = k \cdot \underline{d} \quad (1)$$

where

- n fringe number
- $\lambda$  wavelength of the coherent laser light
- k sensitivity vector  $(i_2 - i_1)$

$i_1$  and  $i_2$  are the unit vectors in the illumination and observation direction respectively and  $\underline{d}$  is the surface displacement vector at the point of observation of the specimen. In the present experimental setup the diffusely reflective surface of the specimen is oriented normal to the bisector of the angle  $2\alpha$ , between  $i_1$  and  $i_2$  (Figure 7). Thus, since the sensitivity vector  $k$ , also points along this bisector, the interferometer senses only the out of plane displacement component,  $w$ . Equation (1) then becomes

$$n\lambda = w2\cos\alpha$$

$$w = \frac{n\lambda}{2\cos\alpha} \quad (2)$$

In the present experimental setup, the surface normal is  $10^{\circ}$  deg. off the observation direction. With  $\lambda = 0.633 \mu\text{m}$ , this shows that each fringe represents an out of plane displacement change of  $0.321 \mu\text{m}$ .

A schematic of the present experimental setup is shown in Fig. 8. Using the newly incorporated recording device we have studied the failure of 2 specimens so far. A considerable amount of experience has been gained with a view toward improving further the experimental setup. One outstanding problem we are presently faced with is the application of load, which we accomplish with the aid of a hand pump to drive the actuator of the loading device. Incorporating a servohydraulic loading system is currently being pursued. Once a test is completed, the recorded interferometric information is replayed and photographs are made from the screen of the TV monitor using a standard 35 mm camera.

#### 2.4. Results and Discussion.

In order to interpret the holographic fringe data presented in this section it is important to understand the procedure by which the photographs are generated. The test specimen is loaded to the reference load  $P_0$  and the valves of the hydraulic system are closed. The hologram is exposed and developed. The valves of the system are opened and the load is increased until the fringe density becomes too great for proper viewing. These steps are then repeated. The difficulty with this procedure is that while the hologram is being produced and the valves of the hydraulic system are closed, the load tends to drop off. This is due to either leakage in the hydraulic system or creep of the test specimen. This is the reason we have decided to replace the hand pump by a servocontrolled loading mechanism which would ensure a more controlled loading. Since there may be a load drop between making a hologram and viewing it in some of the interferometric data presented the reference load state is higher than the load state at which the interferogram was made. One of our main objectives is to understand the spreading of the damage that initiates at the edge of the hole. Thus, this minor drawback in the loading

device should not deter us from extracting some important features that we have captured so far.

For the first sequence of events (i.e. specimen with dimensions 5"x5" see Figure 9). Figure 9b shows the first instance at which a delamination was detected. A delamination appears as a cluster of fringes on the hole edge. Notice that there are some extraneous fringes approximately 3 in number representing a displacement change of  $0.963 \mu\text{m}$ . These are due to a rigid body motion of the specimen coupled with some slight bending. However, these are not to be mistaken with the fringes resulting from an initiated delamination.

The rigid body motion or/and slight bending cannot be totally avoided in a compression test. The slight bending may be the result of any initial imperfection in the specimen. Added to this we must realize that the sensitivity of the technique, which is a function of the wavelength of the laser light, is extremely high (displacement changes as small as  $0.316 \mu\text{m}$  can be detected).

Figure 9b-p shows sequentially the growth and subsequent spreading of the initiated delamination. The initiation occurs at the hole edge at approximately  $90^\circ$  to the load direction and subsequently spreads, with increasing load. Notice the distortion of the fringes around the hole edge. Figure 9p contains a high density of extraneous fringes thus making it difficult to extract any qualitative features regarding the delaminated region. However, this interferogram was included for comparison with Figure 9q which shows the change in fringe pattern with delamination spreading just prior to final failure. Figures 9p and 9q have the same reference load while "q", which is subsequent to "p", demonstrates an area with an extremely high fringe density, so much so that the fringes cannot be resolved. This area then has an out-of-plane displacement change which is much higher than the rest of the plate. Note that in Figure 9p,  $P_s = 1.014 P_f$ , indicating a higher load than the failure load  $P_f$ . This is because  $P_f$  is the catastrophic failure load. The maximum load recorded

during the experiment occurred prior to catastrophic failure.

In the second sequence of interferograms (specimen dimension 3"x3", see Figure 10) the first sign of initiation is seen in Figure 10a. With increasing load the delamination does not show signs of spreading as in the previous case. Instead, we see clearly a symmetric pattern of "delamination spots" around the hole contour (Figures 10a-p). We must point out that, although the interferograms presented in sequence show very little evidence of any difference in the displacement field around the hole edge, viewing the fringes in real time makes it much easier to capture the points at which delamination occur. Thus our discussion is motivated from such a knowledge. In the first test, we recorded an initiation load  $P_I$  of 38,916 lbf while the failure load  $P_P = 44,476$  lbf. In the second test we noticed  $P_I = 24,254$  lbf and  $P_P = 31,724$  lbf. In both cases initiation occurs at 75-87% of the ultimate failure load of the specimen. Notice the difference in the initiation points around the hole contour for the different specimens. While we are not able to offer any explanation for this difference we note the difference in specimen dimensions and more importantly the directional properties.

Summarizing we see that the behavior of the plate can be broken down into a sequence of events. Firstly, when the applied load reaches 75-87% of the catastrophic failure load  $P_P$ , a delamination initiates. Then, with increasing load the delamination spreads around the hole edge, away from the direction of load application. Upon reaching a critical delaminated size the delaminated portion buckles. This is followed by catastrophic failure of the specimen. Notice that we have only addressed the question of failure by delamination. As reported elsewhere [2] other failure mechanisms, such as matrix shearing, is not addressed.

## 2.5. Relation of Analytical Developments to Experimental.

### Observations

The problem of initiation of delamination in laminated composites has received a lot of attention in the literature. Recently, O'Brien-Raju [3] addressed the question of delamination initiation around a circular hole. However, the model, originally developed for straight-edge delamination growth, predicted onset strains about 30% higher than, those experimentally observed. Wang and Choi [4] further extended the earlier work of Pipes and Pagano [5] and found analytically that stress singularities occur along straight free edges. Using Wang's results, Ericsson et al. [6] attempted to predict onset strains for  $[0/90]_s$  laminates with a circular hole. The analysis used total strain energy release rate ( $G$ ) as opposed to separating  $G$  into its components  $G_I$ ,  $G_{II}$ , and  $G_{III}$ . Many other researchers have attempted to obtain the complete 3D stress field using the finite element method (see ref. 7 for example).

The difficulty in obtaining a satisfactory solution to the complete 3D stress field in composites lies in the inherent singularity that is introduced in modelling the laminate as consisting of discrete layers of different material. The usefulness of the singular stress field in predicting delamination initiation has not been established. The initiation problem is also complex, since many parameters enter into the problem. A satisfactory solution to the initiation problem around circular cutouts must display the observed experimental findings. In particular, the position around the hole edge at which initiation occurs, the interface associated with the delamination, and the load level at initiation must be satisfactorily predicted.

Once the delamination initiates it spreads around the hole edge away from the direction of load application. It is felt that the principal mechanism of spreading is by delamination buckling, a phenomenon observed earlier [8] in the spreading of impact damage. However, more experimental evidence is needed to substantiate this claim. A simple analysis based on

an energy method is being developed to calculate the bucking load of an arbitrarily located delamination at the hole edge. Details of this analysis will be available in the future.

## 2.6. Conclusions.

Holographic interferograms showing the behavior of laminated composites containing a circular cutout under inplane compression have been presented. From these observations the behavior of the composite is seen to consist of delamination initiation at the edge of the hole, followed by spreading of the delaminated area leading to catastrophic failure. The applied load at which initiation occurs is about 80% of the catastrophic failure load  $P_F$ .

## 3. DELAMINATION AT A THICKNESS DISCONTINUITY

Experimental and analytical work have continued on the problem of determining the conditions that govern failure at a thickness discontinuity. The experiments are carried out using a simulated stiffener/panel joint shown in Figure 11. A photograph of the test specimen is shown in Figure 12. Previous work on this problem concentrated on the so called "macro failure" conditions. Tests were carried out to determine the axial force,  $N_x$ , failure condition and the bending moment transverse shear,  $M_x/V_x$ , failure condition. It was found that the axial force required to cause failure was so high that its role in the failure of the joint could be assumed to be negligible. The bending/transverse shear tests showed that the moment was the dominate force in the failure condition. Additional failure tests have been carried out as described in the next section. An analysis of the test configuration has been developed and is described in Section 3.2.

### 3.1. Experiments.

A new test was developed that more closely simulates the conditions that occur in a post buckled stiffened panel (ref. 1). This test consists of using the previously described specimen in a column buckling test. In the test, the column is buckled and loaded into the postbuckled range. The loads in the test specimen, shear, axial, and bending moment, are found from the applied load and the configuration of the buckled column.

3.1.1. Description of Tests. The specimen ends are ground to form a V-shape and are supported on V-notched blocks. This simulates simply supported end conditions. A back plate with a tracing paper is kept adjacent to the specimen (Fig. 13) and at various load levels the specimen configuration is traced with a pencil. This curve is used to obtain the deflection and slope of the specimen as a function of load which enables calculating the bending moment and shear force. This procedure is deemed satisfactory by comparing the results obtained with the analysis presented in Section 3.2 which shows good agreement.

3.1.2. Results. In all of the tests initiation of failure in the form of edge cracks appeared at the point of maximum moment. Post experiment examination of the specimen revealed edge cracks between layer 2 and 3 (Figure 14). These delaminations are due to the interlaminar stresses that develop at the free edge. These stresses have been shown to be singular for the idealized problem at the free edge (Ref. 4). It is worthwhile noting that experiments on laminates under tensile loading (Ref. 9) have exhibited a similar failure initiation mechanism. In all of the specimens, these edge cracks grew in the axial direction, but in some specimens failure occurred by rupture at the point of maximum moment. In two of the specimen, the failure occurred by stiffener separation. Figures 15 and 16 show the two types of failure observed in the experiments. The results obtained in the stiffener separation case are plotted along with results from previous experiments (Ref. 1) in Figure 17.

### 3.2. Analysis.

An analysis of the buckling and postbuckling of the simulated joint test specimen was carried out in order to help in evaluation of the experimental data. The usual assumptions of beam theory were made with the properties of the test specimen determined from independent tests. The following sections describe the two analyses.

#### Buckling

The coordinate systems and the nomenclature used for the buckling analysis is shown in Figure 18. It is assumed that at the ends of the column there is no moment. This is simulated in the experiment by the knife edge supports. However, due to the eccentricity of the neutral axes of the two parts of the column, there is a shear force at the ends of the column. This is easily found from overall equilibrium. With the end forces and moments known, the column buckling equations can be written in the second derivative form. These equations are given as follows:

$$(EI)_1 \frac{d^2 v_1}{dx_1^2} = - \frac{Pe}{l} x_1 - Pv_1$$

$$(EI)_2 \frac{d^2 v_2}{dx_2^2} = + \frac{Pe}{l} x_2 - Pv_2$$

The solution of these equations is straight forward, with the results as given below.

$$v_1 = A \sin \lambda_1 x_1 + B \cos \lambda_1 x_1 - \frac{ex_1}{l}, \quad \lambda_1^2 = P(EI)_1$$

$$v_2 = C \sin \lambda_2 x_2 + D \cos \lambda_2 x_2 - \frac{ex_2}{l}, \quad \lambda_2^2 = P(EI)_2$$

The four constants introduced in the solutions are found by the displacement conditions at the ends of the column and the matching of slope and displacement at the thickness step. These conditions and the resulting equations are given below.

$$v_1(0) = 0$$

$$v_1(0) = 0$$

$$v_1(\alpha l) = v_2(1 - \alpha l)$$

$$\frac{dv_1}{dx_1}(\alpha l) = - \frac{dv_2}{dx_2}(1 - \alpha l)$$

$$\begin{bmatrix} \sin \lambda_1 \alpha & -\sin \lambda_2 l(1 - \alpha) \\ l \lambda_1 \cos \lambda_1 \alpha & l \lambda_2 \cos \lambda_2 l(1 - \alpha) \end{bmatrix} \begin{Bmatrix} A \\ B \end{Bmatrix} = \begin{Bmatrix} e \alpha^2 \\ \alpha e \end{Bmatrix}$$

The buckling load is found from the equation developed by setting the determinate of the coefficients equal to zero. This leads to the following transcendental equation which was solved numerically for the particular experimental conditions.

$$(l \lambda_2) \sin(\lambda_1 l \alpha) \cos(\lambda_2 l)(1 - \alpha) + (l \lambda_1) \cos(\lambda_1 l \alpha) \sin(\lambda_2 l)(1 - \alpha) = 0$$

The results for the buckling experiments and the analysis are shown in Table 1. The comparison is satisfactory and lends confidence to both the experiment and the analysis.

#### Post Buckling

The postbuckling analysis is carried out in a manner similar to Euler's Elastica problem (Ref. 10). As in the previous analysis the column is analyzed for the two sections where EI is constant and matching

enforced at the step. The coordinate systems and the nomenclature are shown in Figure 19.

Starting with Section 2, the moment at any point can be written as

$$M = -\frac{Pe}{l}x_2 + Pv_2 = -\frac{(EI)_2}{R} = -(EI)_2 \frac{d\theta}{ds_2}$$

where the expression for curvature,  $R$ , is no longer approximated as in the previous analysis.

Differentiating this expression with respect to  $s_2$  and using the relations between  $v_2$ ,  $s_2$ , and  $\theta$  we obtain:

$$\frac{d^2\theta}{ds_2^2} + \lambda_2^2 \sin\theta = \lambda_2^2 \left(\frac{e}{l}\right) \cos\theta$$

$$\frac{dv_2}{ds_2} = \sin\theta, \quad \frac{dx_2}{ds_2} = \cos\theta, \quad \lambda_2^2 = \frac{P}{(EI)_2}$$

This is the nonlinear differential equation for the right section of the column. Multiplying by  $2d\theta$  and integrating, the following equation is obtained.

$$\int \frac{d^2\theta}{ds_2^2} 2\left(\frac{d\theta}{ds_2}\right) ds_2 + 2\lambda_2^2 \int \sin\theta d\theta - 2\lambda_2^2 \left(\frac{e}{l}\right) \int \cos\theta d\theta$$

or

$$\left(\frac{d\theta}{ds_2}\right)^2 - 2\lambda_2^2 \cos\theta - 2\lambda_2^2 \left(\frac{e}{l}\right) \sin\theta = C$$

The constant  $C$  is determined by using the condition at  $\theta = \phi$ ,  $\frac{d\theta}{ds} = 0$  since the moment is equal to zero at the end.

$$\left(\frac{d\theta}{ds_2}\right)^2 = 2\lambda_2^2(\cos\theta - \cos\phi) + 2\lambda_2^2\left(\frac{e}{l}\right)(\sin\theta - \sin\phi)$$

or

$$ds_2 = - \frac{d\theta}{\sqrt{2\lambda_2} \sqrt{(\cos\theta - \cos\phi) + \frac{e}{l}(\sin\theta - \sin\phi)}}$$

where the negative sign has been chosen for the square root since  $\theta$  decreases as  $s_2$  increases. Assuming that  $e/l$  is a small quantity, an integration over the length  $l_2 = l - \alpha l$  can be performed. In this integration theta goes from  $\phi$  to  $-\psi$  where the angle definitions are positive as given in Figure 19.

$$l_2 = \frac{1}{\sqrt{2\lambda_2}} \int_{-\psi}^{\phi} \frac{d\theta}{\sqrt{(\cos\theta - \cos\phi) + \frac{e}{l}(\sin\theta - \sin\phi)}} \quad (1)$$

A similar expression can be obtained for  $l_1 = \alpha l$

$$l_1 = \frac{1}{\sqrt{2\lambda_1}} \int_{\psi}^{\gamma} \frac{d\theta}{\sqrt{(\cos\theta - \cos\gamma) + \frac{e}{l}(\sin\theta - \sin\gamma)}} \quad (2)$$

The displacements at the step can be found using some of the previously derived expressions. The compatibility condition produces the following result.

$$v_1(l_1) = \frac{\psi}{\gamma} \int dv_1 = \frac{\psi}{\gamma} \int \sin\theta ds_1 = \frac{\psi}{\gamma} \int_{\psi}^{\gamma} \frac{\sin\theta d\theta}{\sqrt{2\lambda_1} \sqrt{(\cos\theta - \cos\gamma) + \frac{e}{l}(\sin\theta - \sin\gamma)}}$$

$$v_2(l_2) = \frac{-\psi}{\phi} \int dv_2 = \frac{-\psi}{\phi} \int \sin\theta ds_2 = \frac{-\psi}{\phi} \int_{\phi}^{-\psi} \frac{\sin\theta d\theta}{\sqrt{2\lambda_2} \sqrt{(\cos\theta - \cos\phi) + \frac{e}{l}(\sin\theta - \sin\phi)}}$$

These expressions may be integrated to give

$$\left(\frac{\lambda_1}{\lambda_2}\right)^2 = \frac{(EI)_2}{(EI)_1} = \frac{\cos\psi - \cos\gamma}{\cos\psi - \cos\phi} \quad (3)$$

Equations (1), (2), and (3) constitute a set of three equations for the four unknowns  $p, \gamma, \psi, \phi$ . In order to solve these equations one unknown must be chosen. In using this analysis for comparison it was decided to use  $\phi$  as the control variable. This was matched to the experiment at the time of failure. The other quantities could then be calculated from the equations developed in the analysis. Some additional rearrangements of these equations were carried out to eliminate the load  $P$  from the equations and to put the elliptic integrals in proper form. Once this was carried out the equations were solved numerically for the unknown angles and the load then determined from equation (1) or (2).

The results of this calculation are given in Table II as well as the comparative experimental quantities. In addition, the displacement at the step is calculated and compared to the experiment.

The agreement between the experiment and the analysis is quite good for this type of problem. This lends confidence to the experimental procedure and to the results for shear and bending moment at failure that are calculated from three experimentally measured quantities.

### 3.3. Conclusions.

The results of the column buckling tests were tainted by the edge delaminations that occurred prior to stiffener separation. Two of the test points were considered reliable and extended the macro failure envelope somewhat (Fig. 17). Continuing to decrease the length of the column would extend the envelope only slightly. Therefore these tests have been discontinued. Other simple tests to extend that failure envelope have not been devised. Future work on this problem will concentrate on plate buckling tests.

#### 4. REFERENCES

1. Babcock, C.D. and Knauss, W.G., "Effect of Stress Concentrations in Composite Structures," Progress Report, SM 84-17. October 1984.
2. Shuart, M.J. and Williams, J.G., "Compression Failure Characteristics of  $\pm 45^{\circ}$  dominated Laminates with a Circular Hole or Impact Damage," 25th SDSM Conference Proceedings, Palm Springs, California, May 14-16, 1984.
3. O'Brien, T.K. and Raju, S.S., "Strain Energy Release Rate Analysis of Delamination Around an Open Hole in composite Laminates," 25th SDSM Conference Proceedings, Palm Springs, California, May 14-16, 1984.
4. Wang, S.S. and Choi, I., "Boundary Layer Effects in Composite Laminates," Parts I & II, Journal of Applied Mechanics, Vol 49, Sept. 1982.
5. Pipes, R.B. and Pagano, N.J., "Interlaminar Stresses in Composite Laminates Under Uniform Axial Extension," Journal of Composite Materials, Vol. 4, 1970, p. 538-548.
6. Ericson, K., Persson, M., Carlsson, L., Gustavsson, A., "On the Prediction of the Initiation of Delamination in a  $[0/90]_s$  and  $[90/0]_s$  Laminate with a Central Circular Hole," Composites Technology Review, Vol. 4, No. 4, Winter 1982, pp. 116-124.
7. Carlsson, L., "Interlaminar Stresses at a Hole in a Composite Member Subjected to in Plane Loading," Journal of Composite Materials, Vol. 17, May 1983.

8. Chai, H., Babcock, C.D., "Two-Dimensional Modelling of Composite Failure in Delaminated Laminates," J. of Composite Materials, Vol. 19, Jan. 1985.
9. O'Brien, T.K. "Characterization of Delamination Onset and Growth in a Composite Laminate," ASTM STP 775, 1982, pp. 140-167.
10. Timoshenko, S.P., Gere, J.M., "Theory of Elastic Stability," McGraw Hill, 1961.

Table 1.  
Buckling Loads of Test Specimens

$$(EI)_1 = 559 \text{ lbin}^2, (EI)_2 = 232 \text{ lbin}^2$$

Specimen #	l(in)	$\alpha$	Buckling Load (lb) Experiment	Buckling Load (lb) Analysis
1	8.00	0.38	38	42
2	9.00	0.33	33	32
3	7.50	0.40	46	49
4	7.25	0.41	47	53
5	7.00	0.43	59	58
6	6.75	0.44	65	63

Table 2.  
Condition at Failure of the Test Specimens

Specimen	$\phi$	$\psi$	$\gamma$	P		$v_2(\alpha)$		
	E	E	A	A		E		
1	54	29	28	40	44	46	1.81	1.73
2	66	42	39	51	37	37	2.25	2.15
3	59	29	27	43	55	55	1.81	1.79
4	60	27	26	43	51	60	1.94	1.77
5	50	21	20	35	66	63	1.44	1.48
6	41	16	15	29	71	67	1.25	1.21

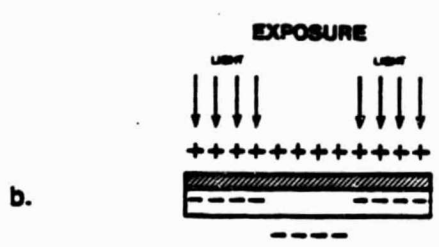
Angles in Degrees, E = Experiment, A = Analysis

22

ORIGINAL PAGE IS  
OF POOR QUALITY



A uniform charge is deposited on the thermoplastic and photoconductor.



Exposure to laser fringe pattern redistributes the charges through the photoconductor.



Recharge increases the electric field across the exposed area of the thermoplastic.



Heating of thermoplastic causes permanent deformation. The irregularities will diffract light to recreate the original image.



Erasure is done by controlled heating.

Figure 1. Process of creating a surface-relief hologram on a thermoplastic plate.

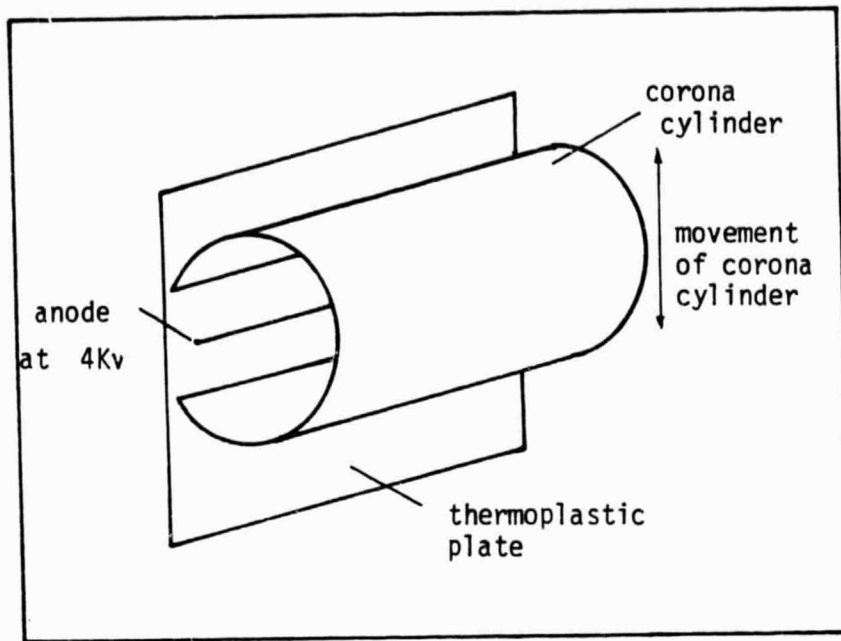


Figure 2. The coronatron deposits a uniform charge on the thermoplastic plate

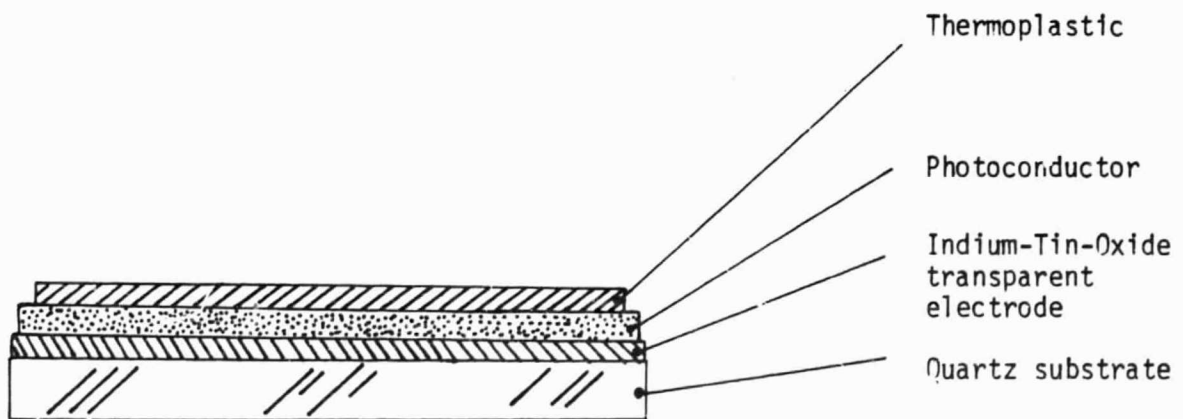
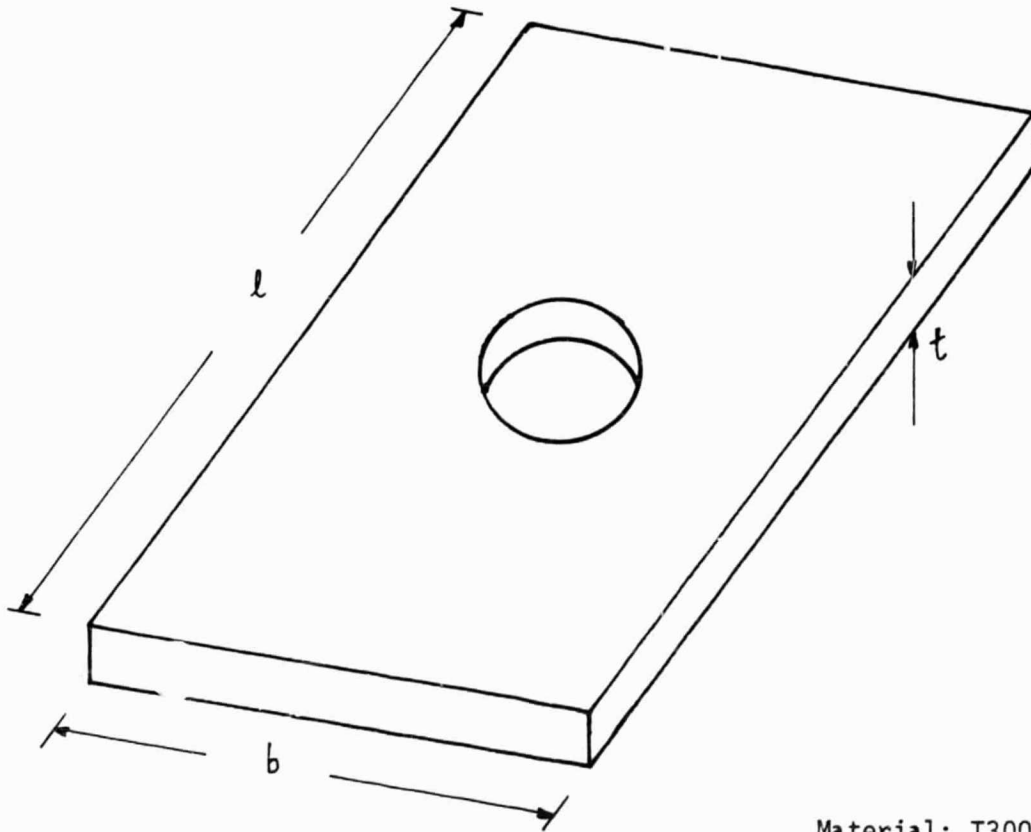


Figure 3. Detailed diagram of thermoplastic plate, showing quartz substrate and transparent electrode.



Material; T300/5208

Specimen #	"l"	"b"	"t"
1	5	5	0.265
2	3	3	0.265

units are in inches.

Hole diameter = 1.0

Figure 4. Perspective of specimen used in compression testing

25

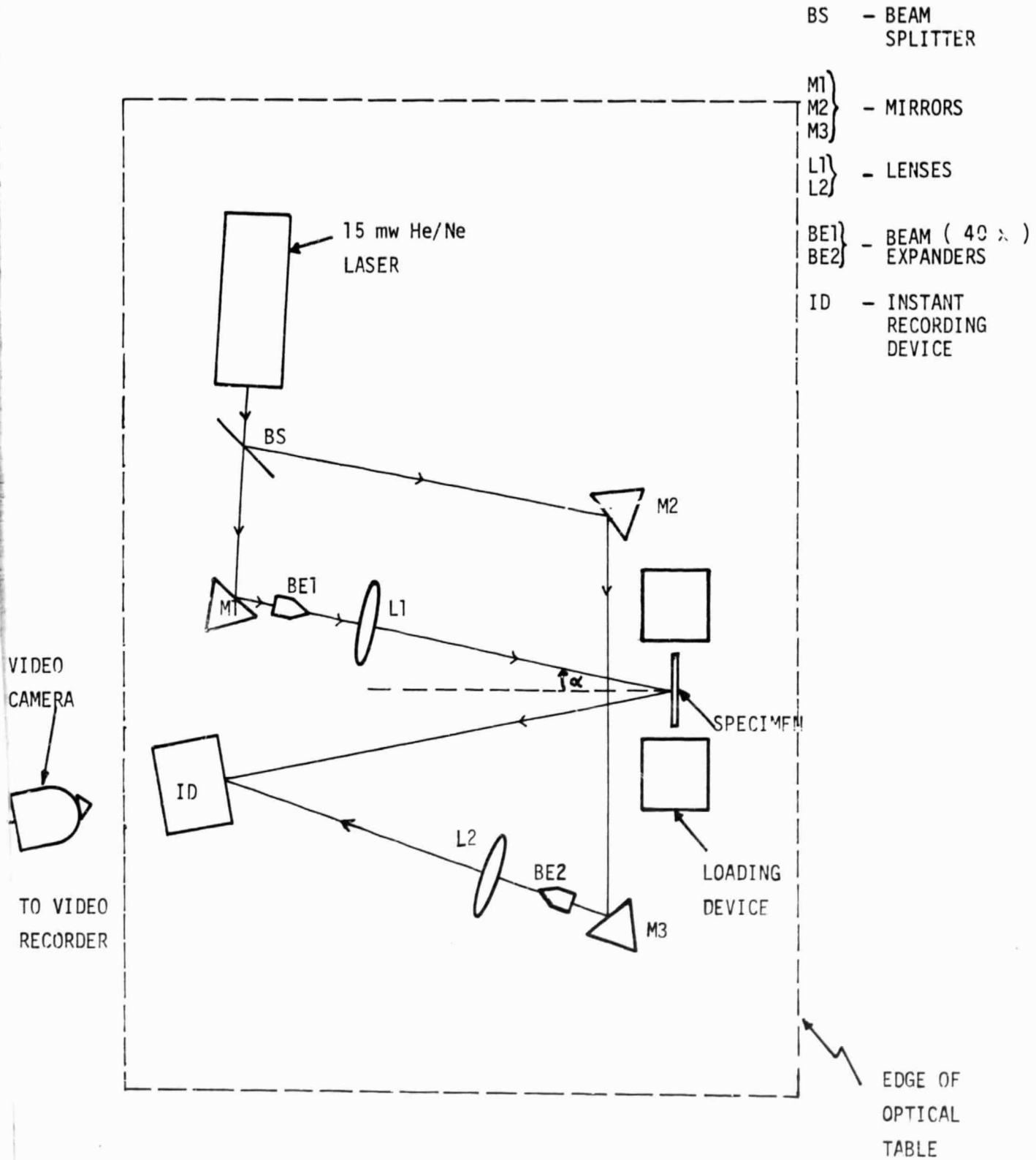
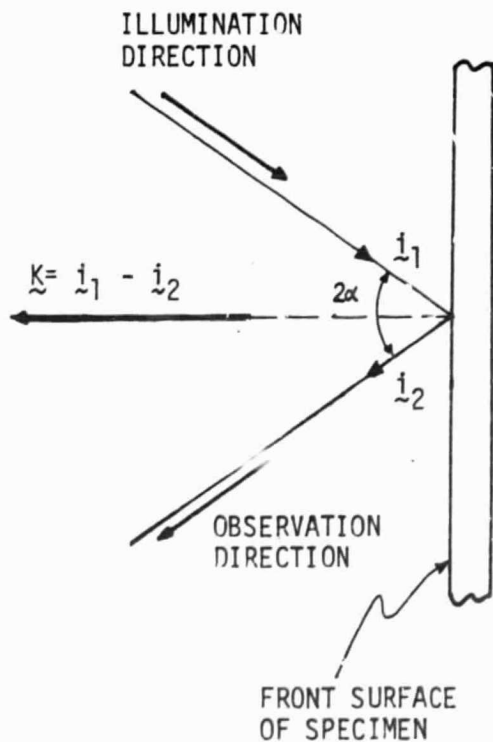


Figure 5. Schematic of Holographic Interferometer.



Figure 6. Hologram showing load cell reading

ORIGINAL PAGE IS  
OF POOR QUALITY



- $\hat{i}_1$  UNIT VECTOR IN ILLUMINATION DIRECTION
- $\hat{i}_2$  UNIT VECTOR IN OBSERVATION DIRECTION
- $\hat{k}$  SENSITIVITY VECTOR

Figure 7. Nomenclature for equations associated with Interferometer.

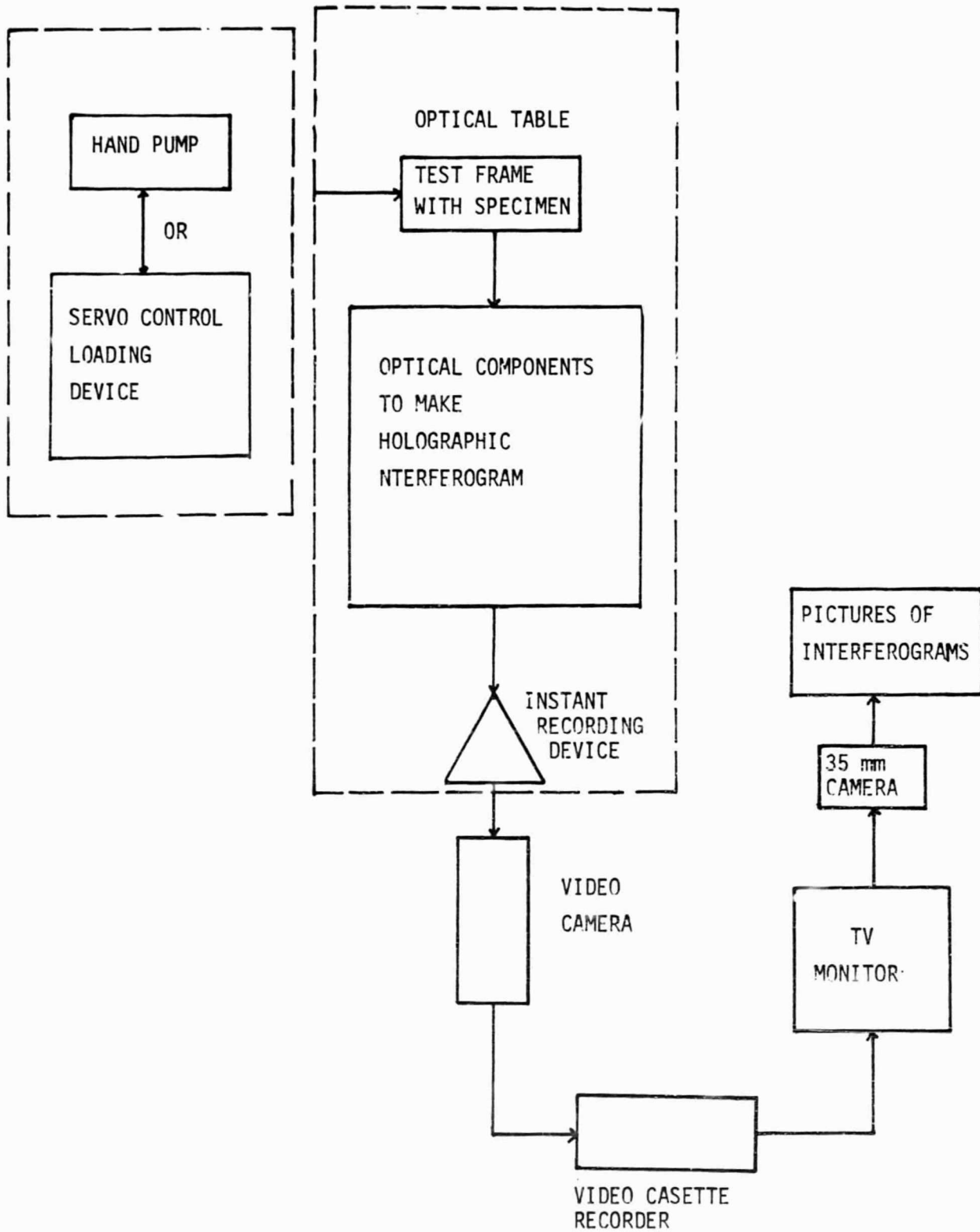
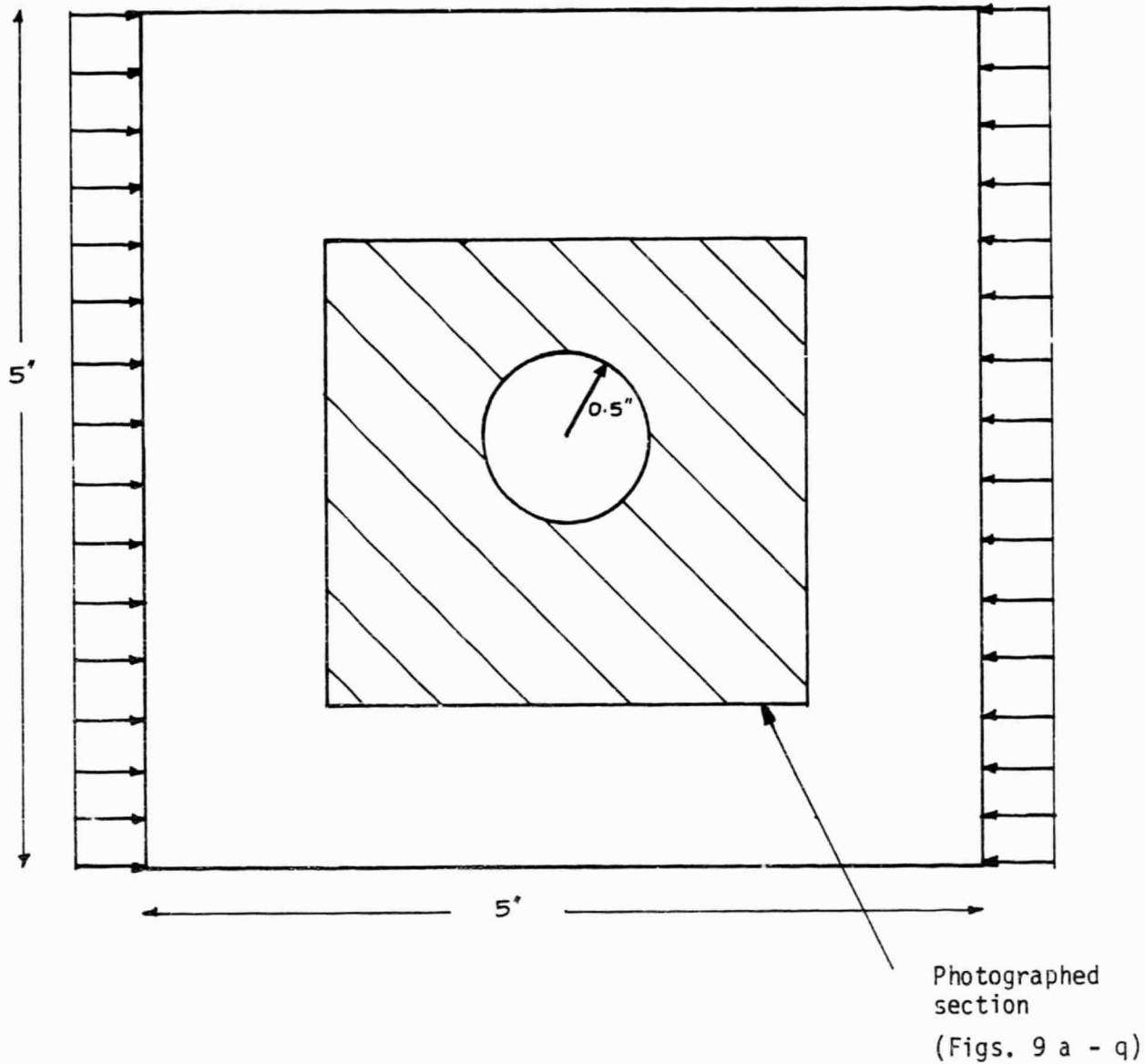


Figure 8. Flow chart of experiment procedure.

28



Specimen ; 1  
Lay up ; (+ 45/90<sub>2</sub>/+45/90<sub>2</sub>/+45/90/0)<sub>2s</sub>  
Failure load (P<sub>f</sub>) ; 44,476 lbf

Figure 9. Data interpretation guide for photos 9 a - q.

## Nomenclature

 $P_f$  = failure load $P_0$  = load carried by the specimen at the time the hologram was made (reference load) normalised by  $P_f$  $P_s$  = load in the specimen corresponding to the interferogram displayed in photograph, normalised by  $P_f$ 

Figure 9 a

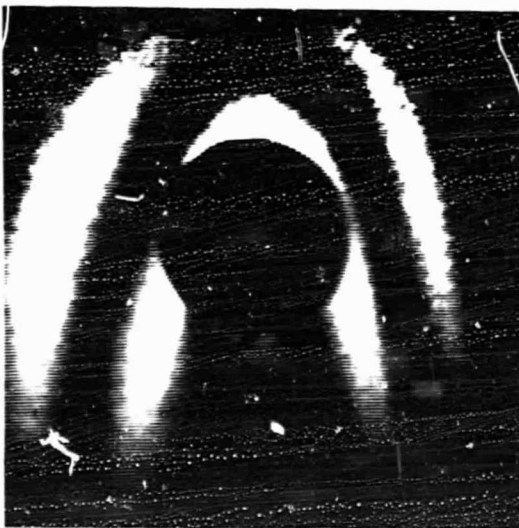
 $P_0 = 0.625$  $P_s = 0.656$  $\Delta P = 0.031$ 

Figure 9 b

 $P_0 = 0.859$  $P_s = 0.875$  $\Delta P = 0.016$

30

ORIGINAL PAGE IS  
OF POOR QUALITY

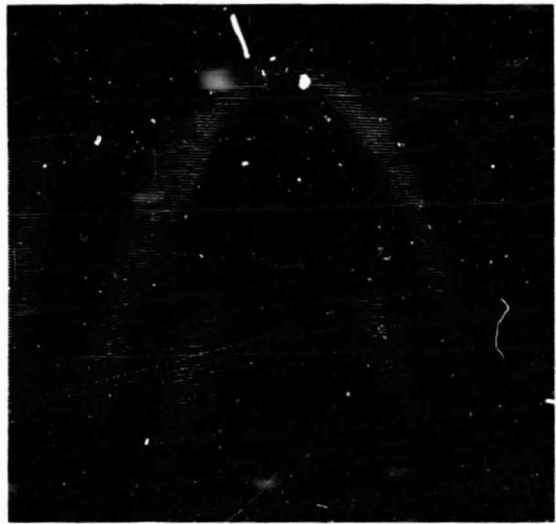


Figure 9 c

$$p_o = 0.859$$

$$p_s = 0.867$$

$$\Delta p = 0.008$$

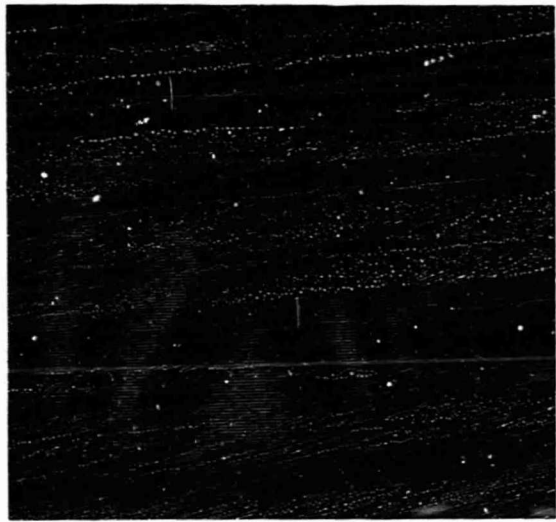


Figure 9 d

$$p_o = 0.930$$

$$p_s = 0.937$$

$$\Delta p = 0.007$$



Figure 9 e

$$p_o = 0.953$$

$$p_s = 0.953-0.883$$

$$\Delta p = 0-0.07$$

ORIGINAL PAGE IS  
OF POOR QUALITY

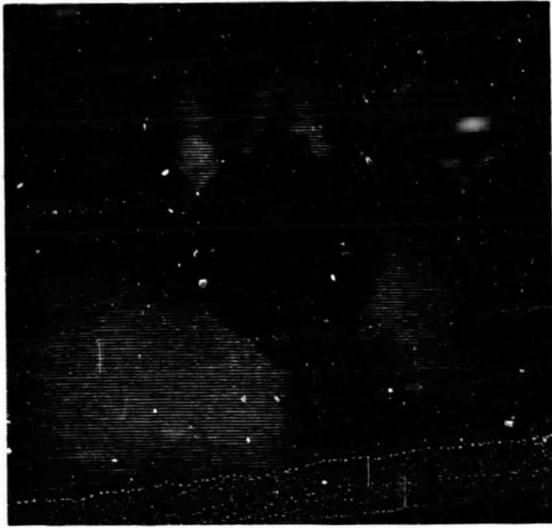


Figure 9 f

$$p_o = 0.953$$

$$p_s = 0.953 - 0.883$$

$$\Delta p = 0 - 0.07$$

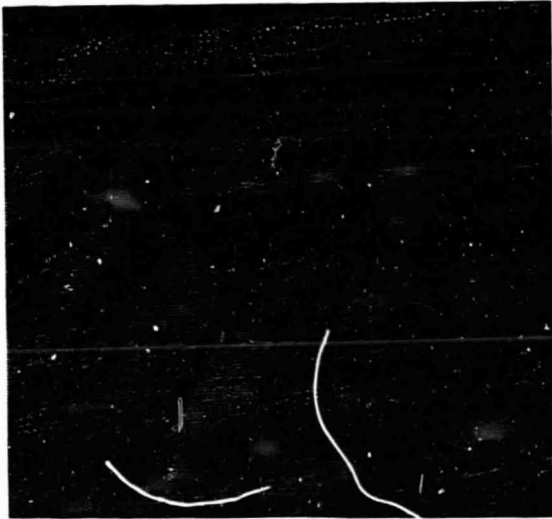


Figure 9 g

$$p_o = 0.883$$

$$p_s = 0.891$$

$$\Delta p = 0.008$$



Figure 9 h

$$p_o = 0.883$$

$$p_s = > 0.891$$

$$\Delta p = > 0.008$$

32

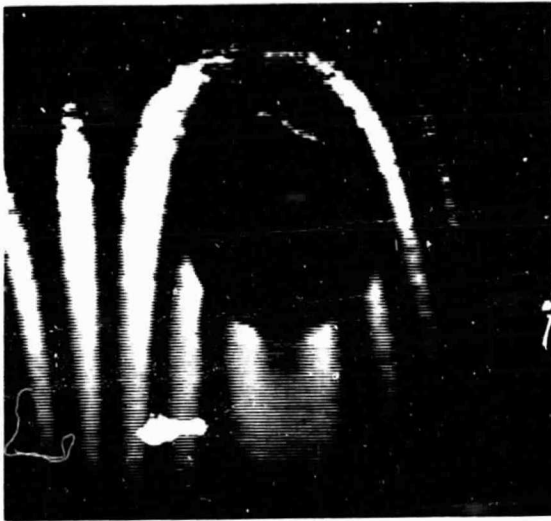


Figure 9 i

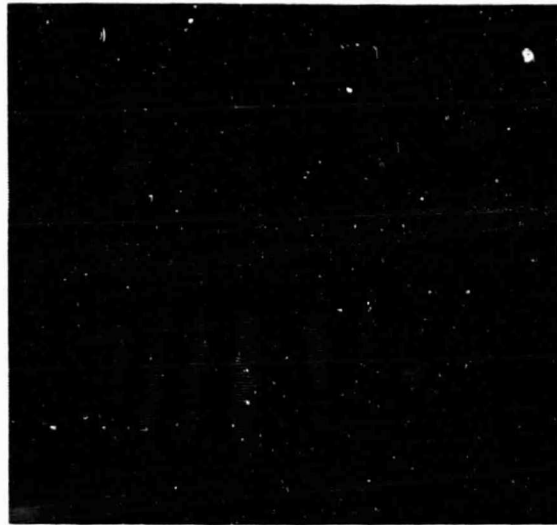


Figure 9 j

Figures 12i - 1

$$\begin{aligned} p_o &= 0.984 \\ p_s &= 0.969 - 1.0 \\ \Delta p &= \pm 0.016 \end{aligned}$$

ORIGINAL PAGE IS  
OF POOR QUALITY



Figure 9 k



Figure 9 l

ORIGINAL PAGE IS  
OF POOR QUALITY

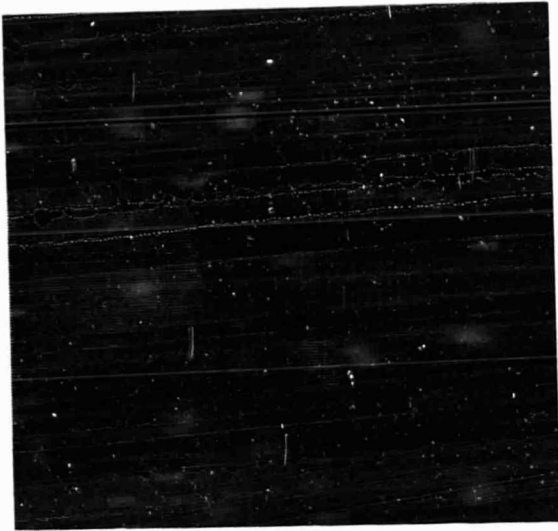


Figure 9 m

$$p_o = 0.984$$

$$p_s = 0.969 - 1.0$$

$$\Delta p = \pm 0.016$$



Figure 9 n

$$p_o = 0.984$$

$$p_s = 0.969 - 1.0$$

$$\Delta p = \pm 0.016$$

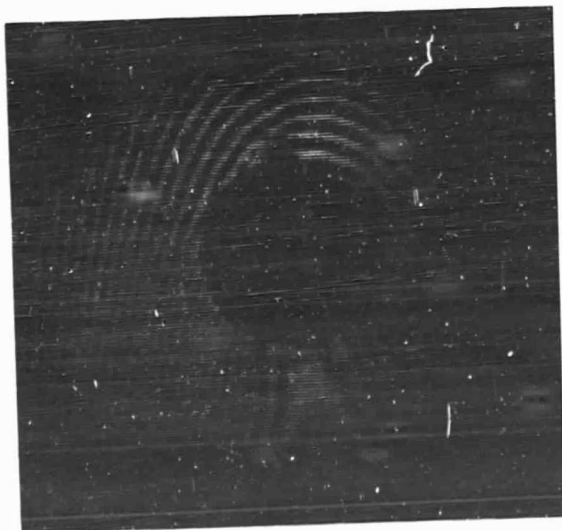


Figure 9 p

$$p_o = 1.0$$

$$p_s = 1.023$$

$$\Delta p = 0.023$$

34

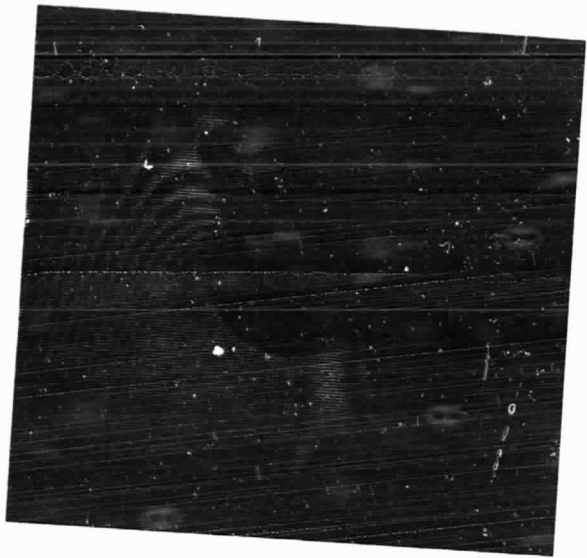


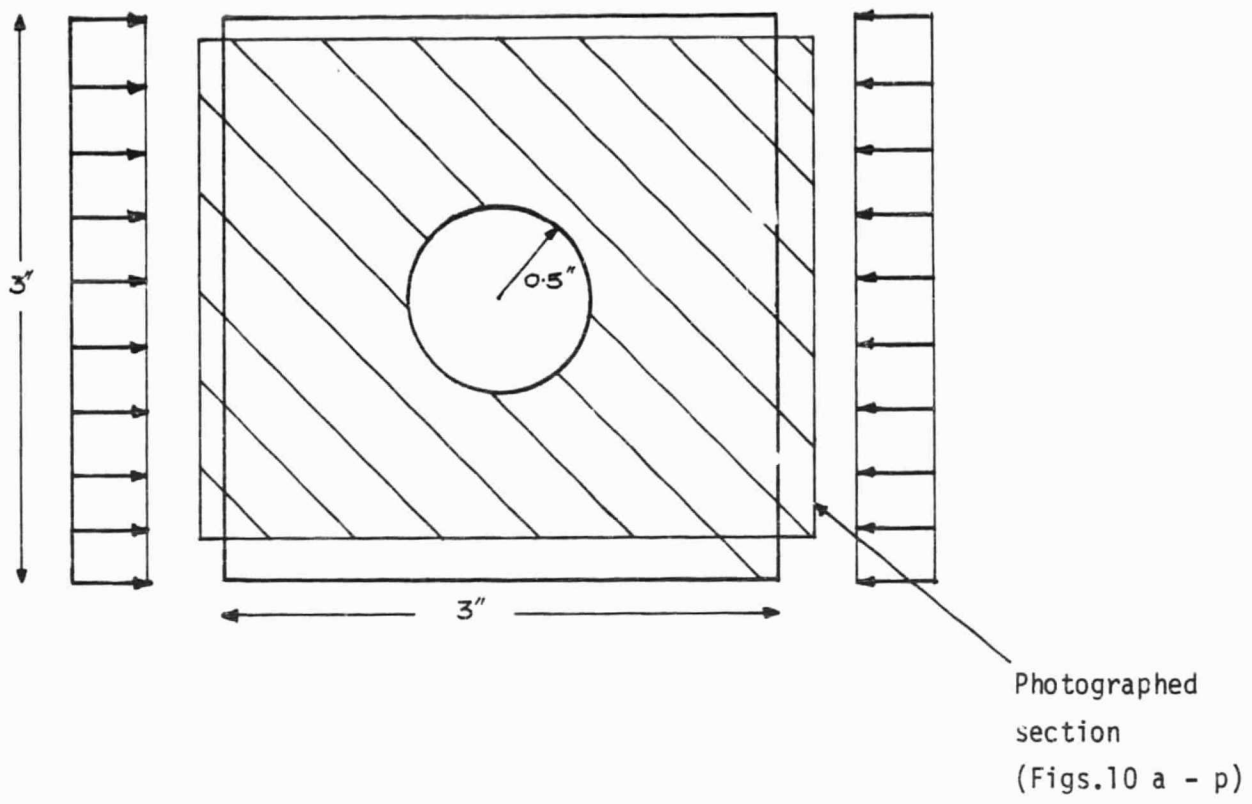
Figure 9 q

$$P_0 = 1.0$$

$$P_s = ?$$

$$\Delta P = ?$$

35



Specimen ; 2  
Lay up ; (-45/0<sub>2</sub>/-45/0<sub>2</sub>/-45/0/90)<sub>2s</sub>  
Failure load (p<sub>f</sub>) ; 31,724 lbf

Figure 10. Data interpretator, guide for photos 10 a - p.

ORIGINAL PAGE IS  
OF POOR QUALITY



Figure 10 a

$$p_0 = 0.778$$

$$p_s = 0.765$$

$$\Delta p = -0.073$$

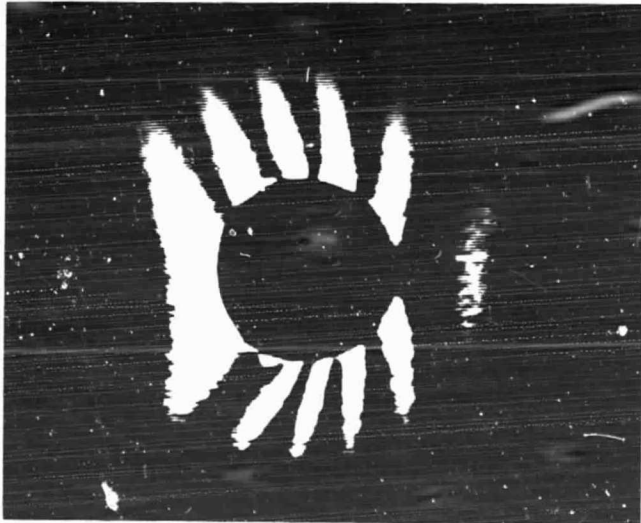


Figure 10 b

$$p_0 = 0.786$$

$$p_s = 0.773$$

$$\Delta p = -0.013$$

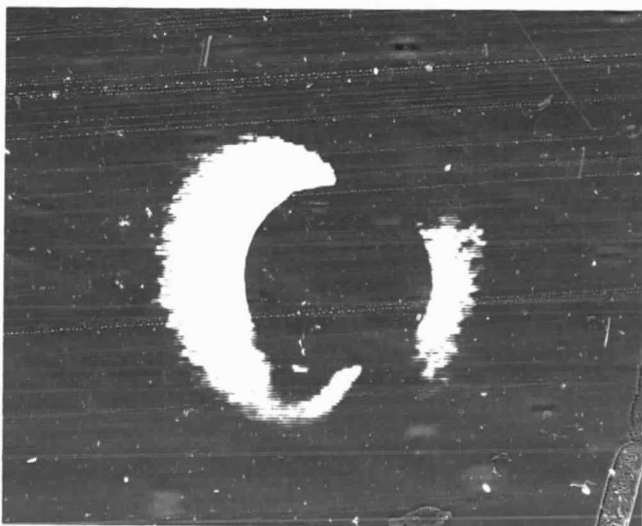


Figure 10 c

$$p_0 = 0.786$$

$$p_s = 0.774$$

$$\Delta p = -0.012$$

37

ORIGINAL PAGE IS  
OF POOR QUALITY

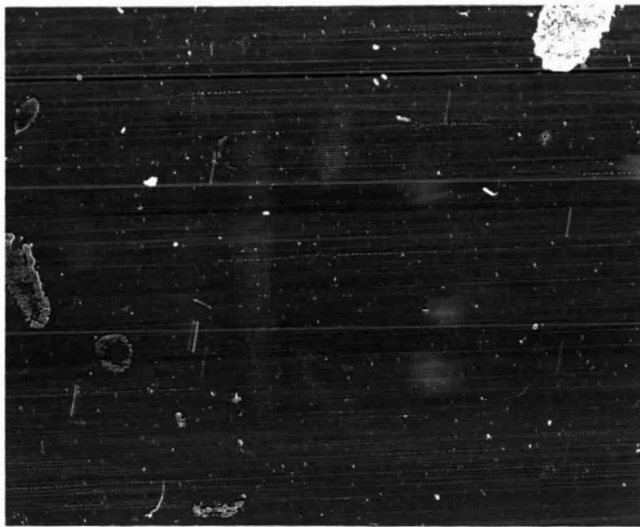


Figure 10 d

$$p_o = 0.786$$

$$p_s = 0.777$$

$$\Delta p = -0.009$$



Figure 10 e

$$p_o = 0.786$$

$$p_s = 0.781$$

$$\Delta p = -0.005$$

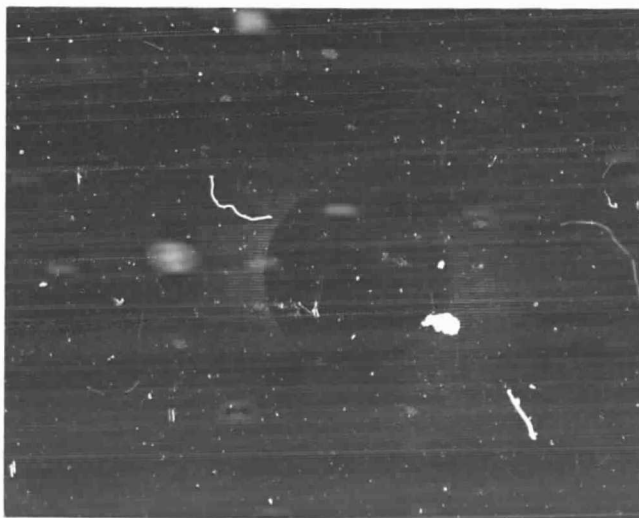


Figure 10 f

$$p_o = 0.777$$

$$p_s = 0.778$$

$$\Delta p = 0.001$$

38

ORIGINAL PAGE IS  
OF POOR QUALITY

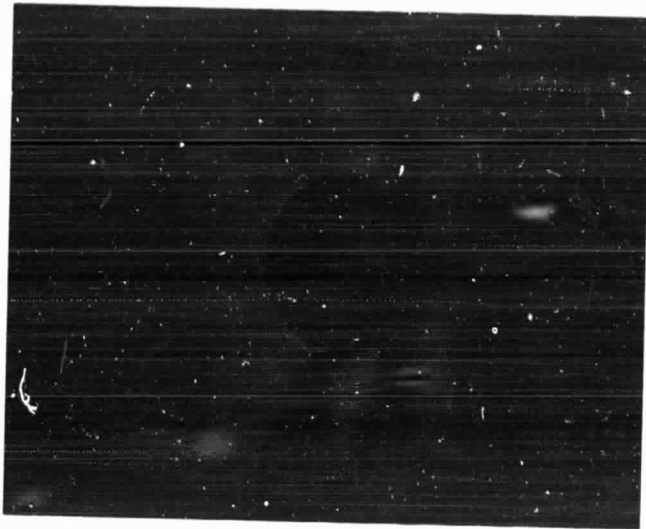


Figure 10 g

$$p_o = 0.777$$

$$p_s = 0.778 - 0.776$$

$$\Delta p = \pm 0.001$$

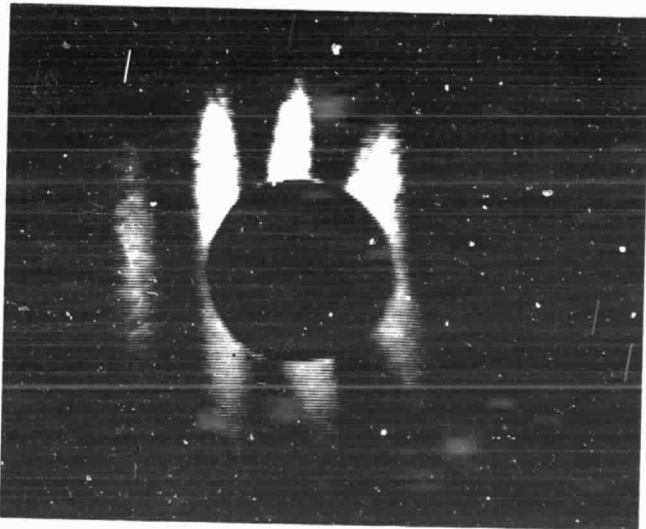


Figure 10 h

$$p_o = 0.786$$

$$p_s = 0.785$$

$$\Delta p = -0.001$$



Figure 10 i

$$p_o = 0.808$$

$$p_s = 0.808$$

$$\Delta p = -0.003$$

ORIGINAL PAGE IS  
OF POOR QUALITY

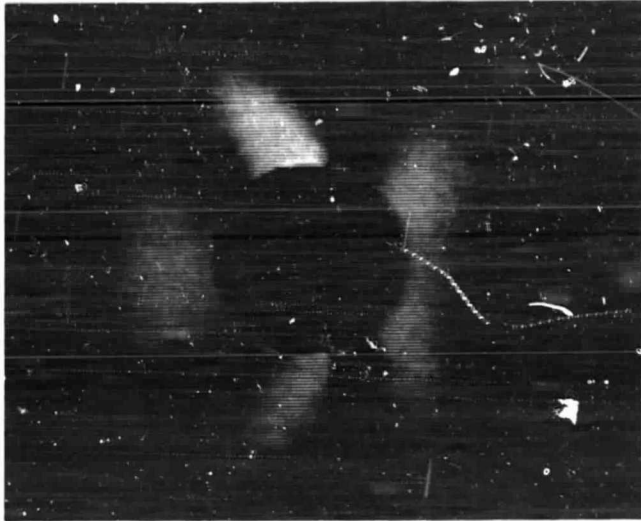


Figure 10 j

$$p_0 = 0.825$$

$$p_s = 0.818$$

$$\Delta p = -0.007$$

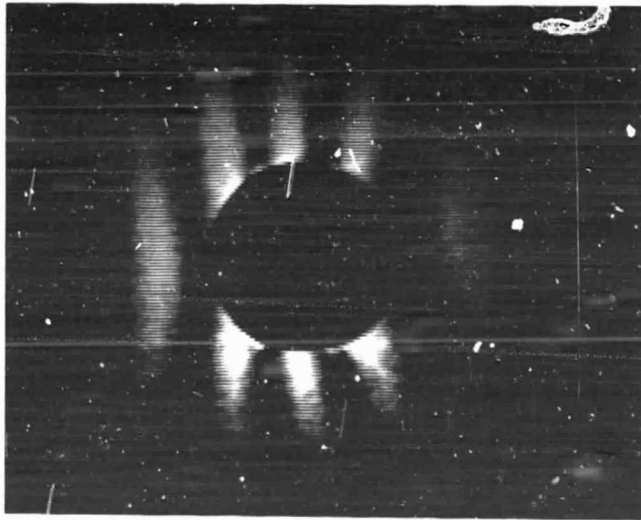


Figure 10 k

$$p_0 = 0.832$$

$$p_s = 0.830$$

$$\Delta p = -0.002$$

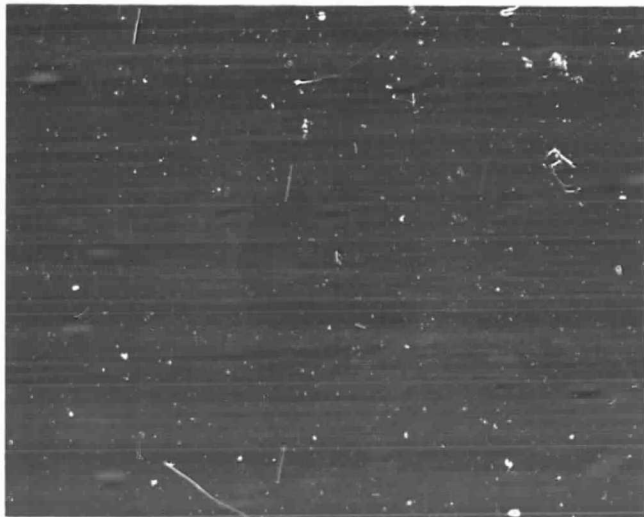


Figure 10 l

$$p_0 = 0.849$$

$$p_s = 0.848$$

$$\Delta p = -0.001$$



Figure 10 m

$$p_0 = 0.849$$

$$p_s = 0.848 - 0.850$$

$$\Delta p = \pm 0.001$$

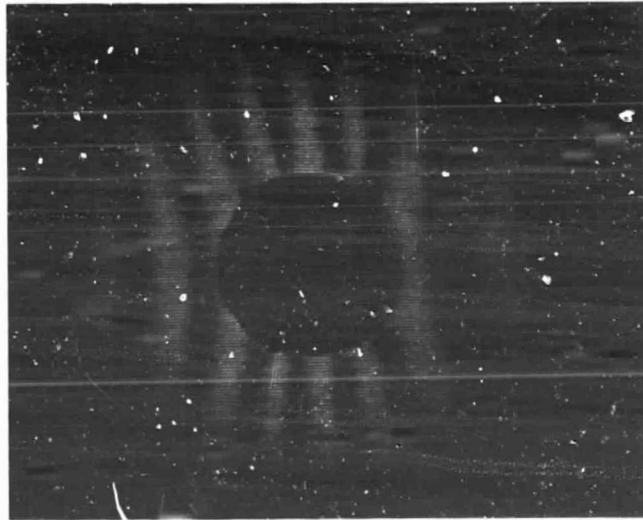


Figure 10 n

$$p_0 = 0.875$$

$$p_s = 0.831$$

$$\Delta p = -0.044$$

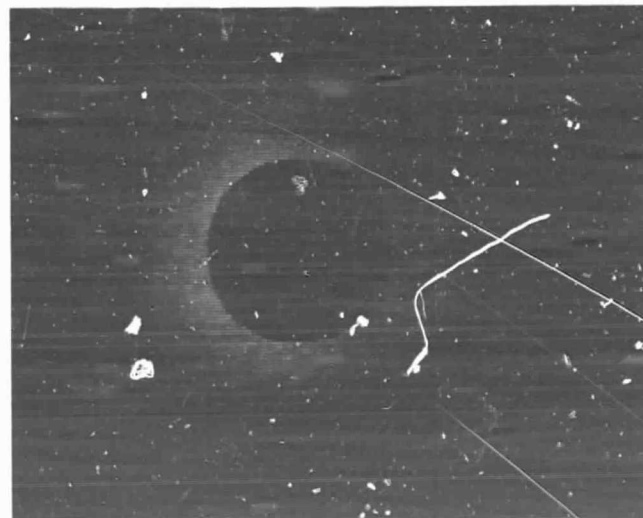


Figure 10 p

$$p_0 = 0.953$$

$$p_s = 1.014$$

$$\Delta p = 0.061$$

(fringe density too high)

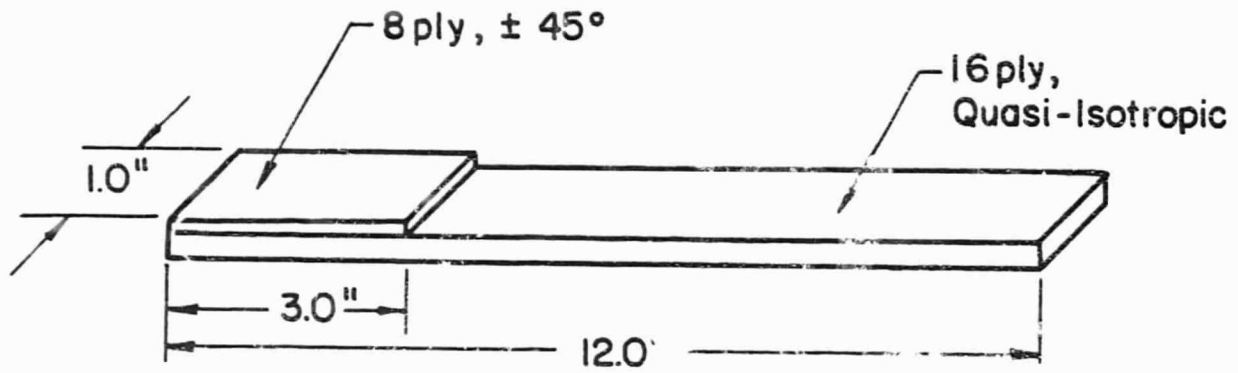


Figure 11. Stiffener delamination test specimen.

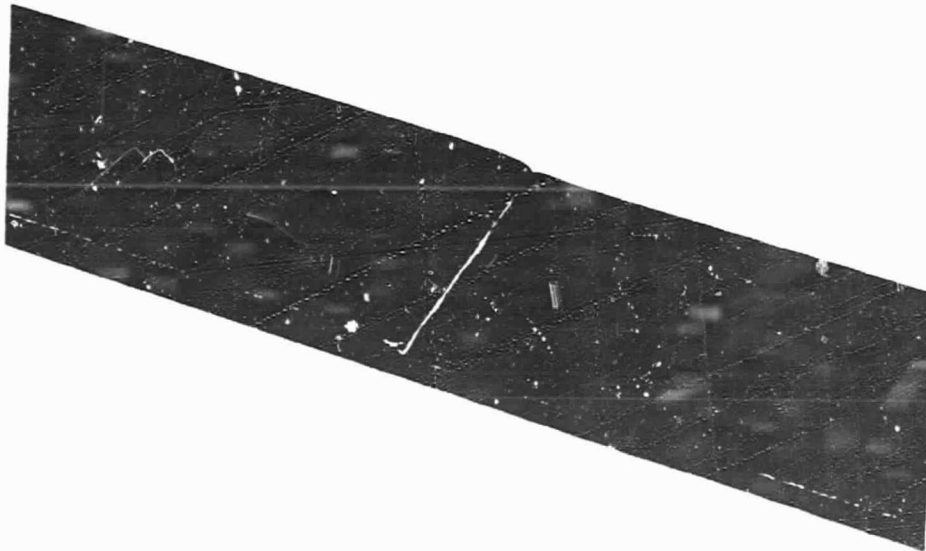


Figure 12. Simulated stiffener joint.

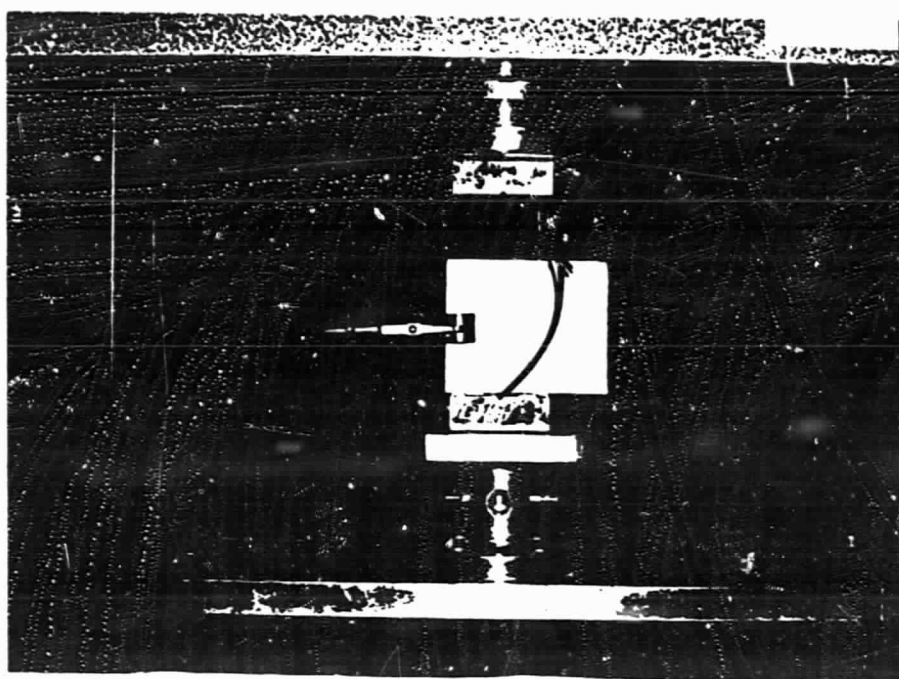
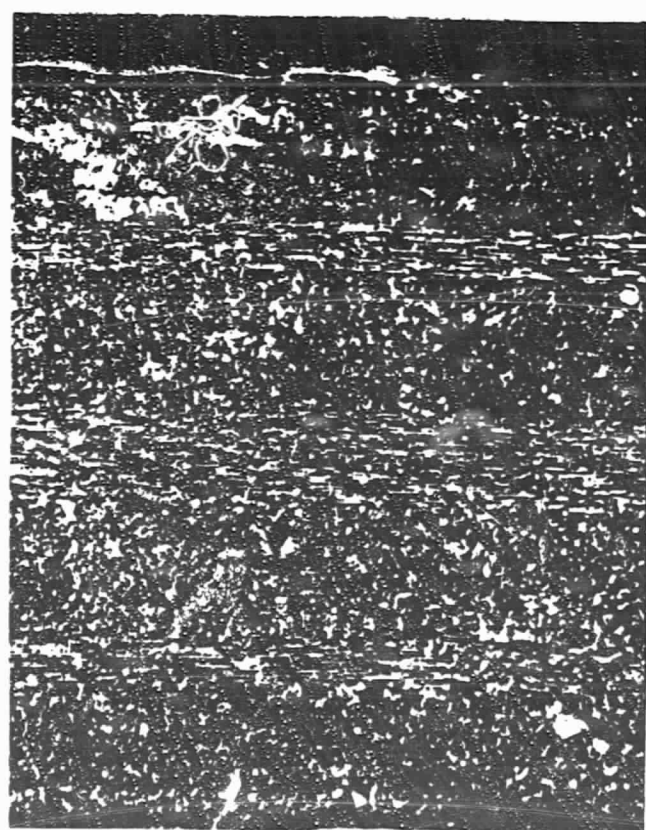


Figure 13. Backplate used to trace specimen configuration.



- 1
- 2
- 3
- 4
- 5
- 6
- 7
- 8
- 9
- 10
- 11
- 12
- 13
- 14
- 15
- 16

Figure 14. Photo showing edge cracks visible between layers 2 & 3.



Figure 15. Sketch of specimen with panel failure. No visible damage to the joint.

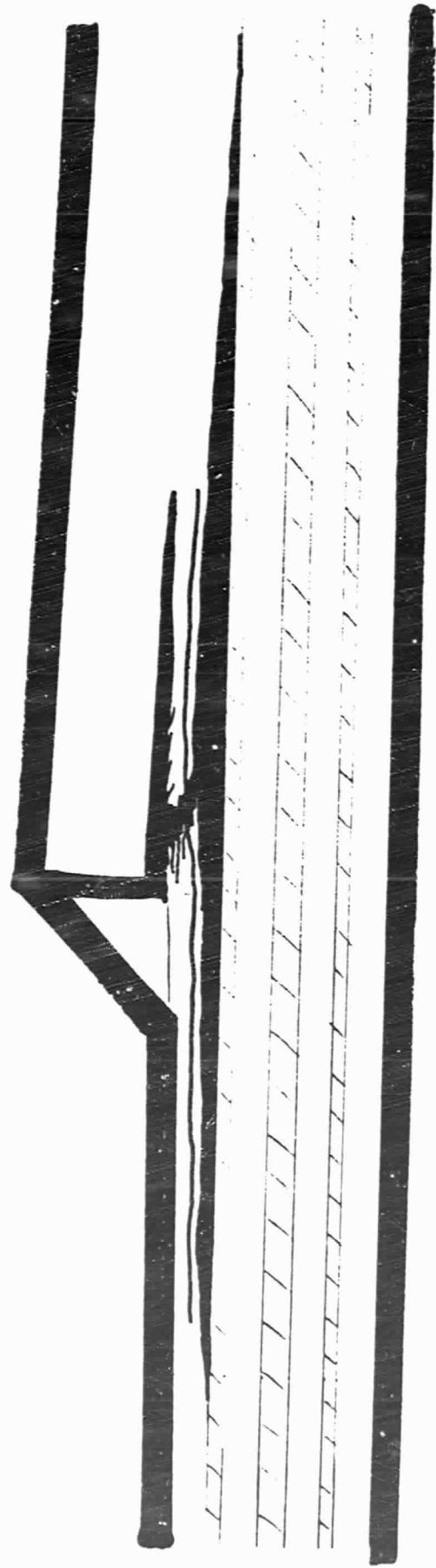


Figure 16. Sketch of stiffener separation failure. The major crack is between layers 3 & 4.

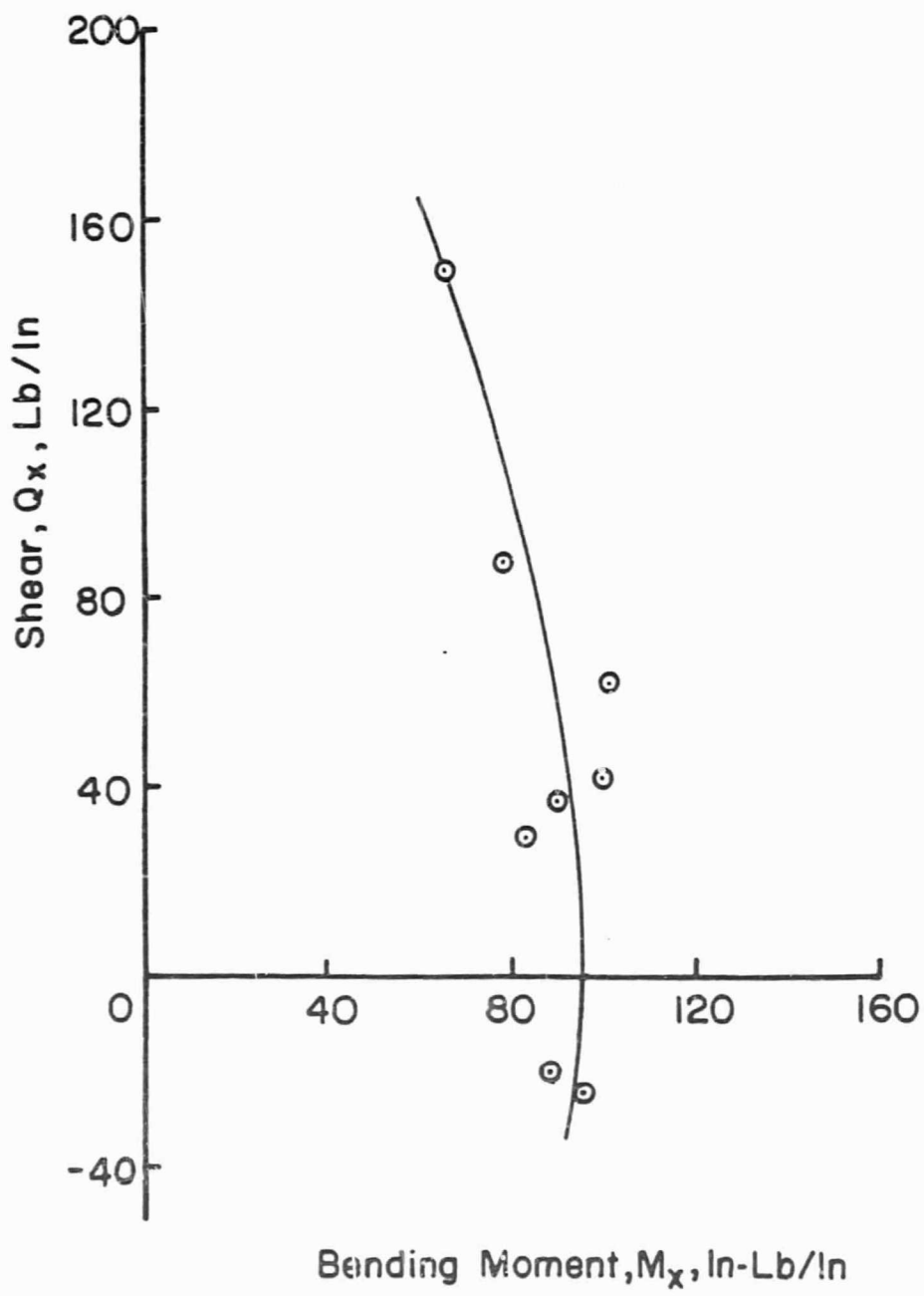


Figure 17. Bending Moment-Shear Failure Envelope

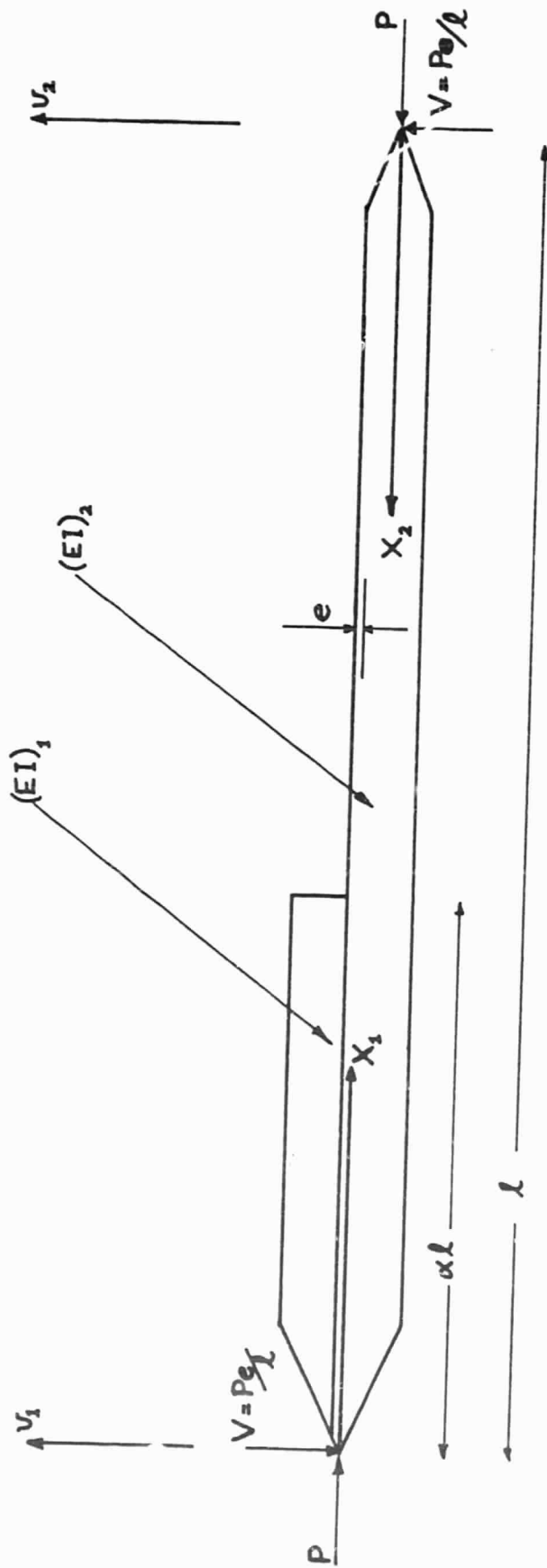


Figure 18. Column geometry and coordinate system.

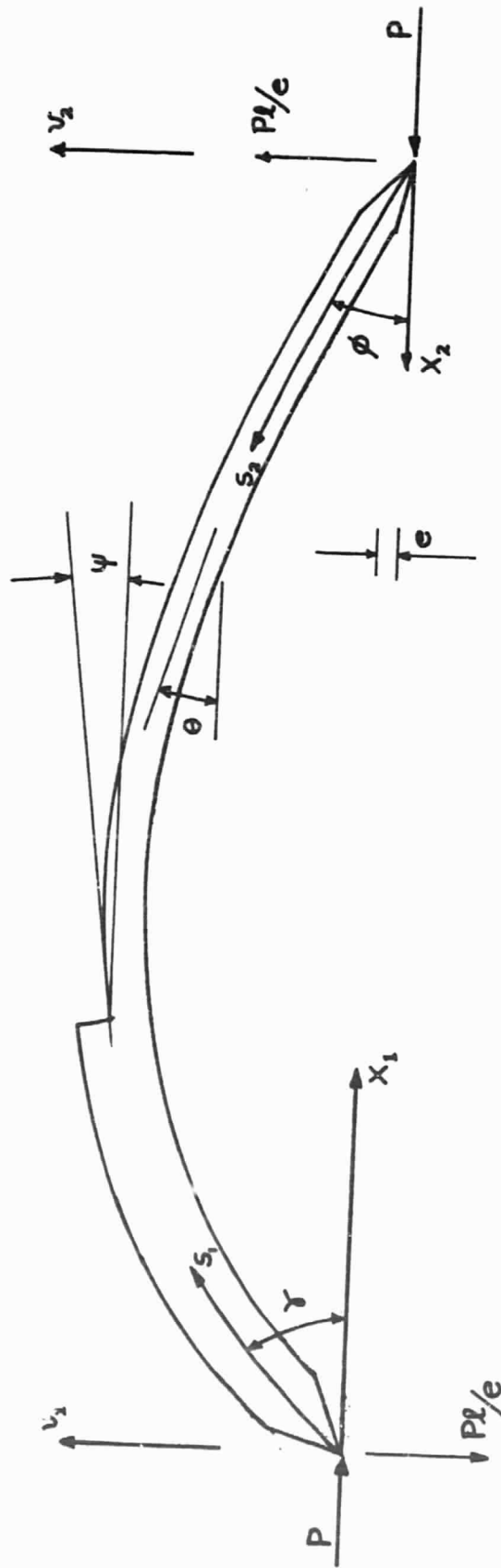


Figure 19. Nomenclature for the non-linear (post buckled) problem.